INTERNATIONAL JOURNAL OF COMPUTERS COMMUNICATIONS & CONTROL
Online ISSN 1841-9844, ISSN-L 1841-9836, Volume: 19, Issue: 6, Month: December, Year: 2024
Article Number: 6862, https://doi.org/10.15837/ijccc.2024.6.6862

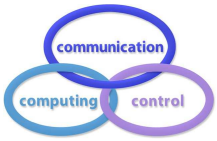

CCC Publications

COVID-19 lung infection segmentation from CT imaging using statistics and edge-region-based active contour

Sorin Curila*, Ioan Buciu, Cristian Grava, Daniel Nistor Trip, Oreste-Mihai Straciuc

Sorin Curila
Dept. of Electronics and Telecommunications
Faculty of Electrical Engineering and Information Technology
University of Oradea
410087, Oradea, Romania
*Corresponding author: sorincurila2015@yahoo.com

Ioan Buciu
Dept. of Electronics and Telecommunications
Faculty of Electrical Engineering and Information Technology
University of Oradea
410087, Oradea, Romania
ibuciu@uoradea.ro

Cristian Grava
Dept. of Electronics and Telecommunications
Faculty of Electrical Engineering and Information Technology
University of Oradea
410087, Oradea, Romania
cgrava@uoradea.ro

Daniel Nistor Trip
Dept. of Electronics and Telecommunications
Faculty of Electrical Engineering and Information Technology
University of Oradea
410087, Oradea, Romania
dtrip.uo@gmail.com

Oreste-Mihai Straciuc
Faculty of Medicine and Pharmacy
University of Oradea
410073, Oradea, Romania
straciuc.orestemihai@didactic.uoradea.ro

Abstract

As of October 2024, the number of global confirmed cases of COVID-19 goes beyond 776 million, with over 7 million deaths, according to World Health Organization (WHO) website. This scarring figure has led to an impressive effort from the medical community, in the attempt to early detect the signs of the infection. Whereas the Reverse Transcription Polymerase Chain Reaction (RT-PCR) testing protocol is being used to detect the infection, medical imaging plays an important role to evaluate the level of lung's damage caused by the presence of the virus. Both computed tomography (CT) and chest radiographs (CXR) have been utilized for laboratory testing by radiologist to identify and measure the affected lung area by isolating the region of interest (ROI). Manual segmentation of ROI is a complex process requiring extensive time and experienced medical staff. Therefore, there is an urgent need of automated assisted medical tools that accurately measure the infected areas and reduce the manual annotation time. An impressive amount of approaches have been proposed to detect the infection or to segment the infected areas, where most of the proposed techniques rely on deep learning (DL). In this work, an alternative to DL is proposed, that is based on several steps, including statistical measures. More precisely, in the first step, the image is coarsely segmented by using an electromagnetism optimization based multilevel thresholding. The multilevels are a priori estimated with the help of Gaussian mixture models (GMM). Next, a morphological skeleton is constructed for the basis of a localized edge-region-based active contour model considering multi-class segmentation. The segmented class is reevaluated and correction step is performed if necessary, i.e. if the number of components is wrongly estimated. The experiments indicate very promising results, the approach performing similar to recent state-of-the-art methods.

Keywords: COVID-19, infection segmentation, CT imaging.

1 Introduction

The complications of Covid-19 infection are manifested by inflammatory response or even failure of body organs. Potential respiratory problems including chronic cough, fibrotic lung disease, bronchiectasis, and pulmonary vascular disease can also be present, leading to anatomical changes in the lung. Those parenchymal abnormalities are visible on CT scans in the form of ground-glass opacity (GGO), consolidation, or pleural effusion (PE) [1], [2]. It was reported that GGO or consolidation were all common in the early rapid progressive stage, GGO and consolidation dominating the advanced stage, and GGO with consolidation decreasing in the recovery stage when the abnormality is gradually absorbed [3].

Most of the work concerning COVID - 19 lung infection detection from CT imagery can be split into three main directions, namely, binary diagnosis (presence or absence of COVID - 19) [4], [5], [6], [7], segmentation and quantification of the abnormal lung opacities [8], [9], and distinguishing COVID-19 from non- COVID-19 pneumonia [10].

2 Related Works

2.1 Classification versus segmentation

The remarkable success of deep learning (DL) based artificial intelligence (AI) in various computer vision tasks [12] has attracted an increased interest in medical image analysis. Covid-19 related approaches are dealing either with detection followed by classification of infected areas or segmentation task. In the classification task the system automatically decides whether or not the image contains infected areas, without considering the severity of the infection (i.e. GGO, consolidation, PE). On the other hand, segmentation addresses the task to find the location of the infection by estimating a segmentation mask.

Most of the approaches are dealing with classification to predict the existence or absence of Covid-19 infection in the lung imagery. Several DL architectures have been applied for COVID-19 CT diagnosis, such as EfficientNet [10], U - Net [13], or ResNet [14]. [21] employed a generative adversarial network to generate more CT images in order to enhance the accuracy. A multi-task multi-slice 3D DL system was proposed by [20] by utilizing two 2D CNN networks, one at slice-level and one at patient-level to learn spatial and temporal features. A DL network augmented with t-distributed

Stochastic Neighboring Embedding and Gradient-weighted Class Activation Mapping is proposed by [19] to enhance the visualization of infected areas. More recently, [18] extended the ResNet50 (a deep residual network) by incorporating a mutex attention block, a fusion attention block and a Res-Layer to achieve 96.98 %accuracy. Finally, Pham [23] compared 16 pretrained CNNs for classification of COVID-19 finding out that DenseNet-201 was the best in terms of accuracy, balance between sensitivity and specificity, F-1 score, and area under curve. A direct comparison between two DL methods, namely, SegNet and U-NET was carried out in [24]. Their experiments indicated that SegNet performs the best for binary task (Covid-19/ Non Covid-19), whereas U-NET showed superior performance for multi-class task.

Segmentation task brings the diagnosis at pixel level to further provide the location of the infection by constructing a lesion mask. The 2D U-Net deep learning architecture [16] successfully employed for lung segmentation, was also recently extended to COVID - 19 segmentation in [17]. [15] proposed a semisupervised approach to segment Covid-19 areas from CT lung scans, where limited labeled images were used to train an Inf-Net CNN model. An image-dependent multilevel image thresholding method is proposed by [22] to segment COVID-19 infected lung regions from chest CT scans. Prior to segmentation they applied an image contrast enhancement algorithm by combing linear and logarithmic stitching parametric algorithms. Edge information is addressed in [26] to form an edge supervised module based CNN followed by an auxiliary semantic supervised module. Multiple scale feature maps at different image levels are fused with an attention module to link high-level and low-level feature maps. A similar network was proposed by [27] where a multiple scale module was designed to sense features at different scales, followed by dense path module to remove semantic gap between features. The detected features are finally fused by an attention module. COV-TransNet is a dual branch fusion network composed of global map and local feature information augmented with a multi-scale attention module [25]. [28] expanded UNet by considering a dual attention model where the channel and position attentions was fused.

2.2 Deep learning versus machine learning

Deep and machine learning are two approaches embraced by most authors as these techniques have proven to perform close to human decisional factors or even leading to superior results compared to human based diagnosis. For DL approaches, the most common employed network is based on variants of CNN as feature extractor, followed by softmax or combination with other modules as classifier. For example, a softmax is combined with a decision tree and Adaboost in [30]. In another example, [29] employed an aggregated residual transformations to learn a robust feature representation and applied the soft attention mechanism to achieve the automated segmentation of multiple COVID-19 infection regions. In [32] the lung region was segmented with a 2D U-Net and the diagnosis of COVID-19 with a hybrid active learning strategy, which simultaneously considers sample diversity and predicted loss. The authors reported an accuracy of over 95 % with using only 30 % of labeled data for training. A joint classification-segmentation system was proposed in[31], where fine grained lesion areas are discovered, while [33] developed a dual-branch combination network (CBN) that can simultaneously achieve individual-level classification and lesion segmentation. Federated semi-supervised learning is proposed in [34] to handle variability in both the data and annotation across several a multi-national database.

Some authors use machine learning approach to Covid-19 diagnosis. Most work was mainly focused on the classification task. For example, [35] uses a set of handcrafted location-specific features. An infection size-aware random forest method (iSARF) was proposed for discriminating COVID-19 from pneumonia. A set of 34 statistical texture features of COVID-19 from ground-glass opacities ROI images were extracted, including 13 gray-level co-occurrence matrix (GLCM) features, 15 gray-level-gradient co-occurrence matrix (GLGCM) features and 6 histogram features in [36]. To separate COVID-19 based lesion from pneumonia, ultimately, the ReliefF algorithm was leveraged to select features with discriminative potential. Logistic regression and random forests are proposed in [37]. ML based Covid - 19 lession segmentation is less represented in the literature. [39] combined a superpixel generation algorithm with a density-based region segmentation algorithm. A set of morphological features are next extracted from each of the extracted nodule regions. The nodule candidate regions

are then classified into the nodule and non-nodule decision using a nonlinear support vector machine (SVM) classifier. Features are characterized by Gray Level Co-Occurrence Matrix (GLCM) that are further classified with SVMs in [40]. However, we should draw attention that these reports were rather dealing with nodule (cancer) segmentation and detection and do not specifically involve Covid-19 lesion segmentation, could be tailored to handle Covid-19 task, though. The closest work considering Covid-19 lesion segmentation can be found in [41]. The approach starts by dividing the CT image into three areas by three threshold segmentation functions, to start with lung segmentation and a coarse GGO segmentation. Next, a contrast function is applied to refine the contour of GGO. Finally, the segmentation result of GGO is combined with the segmentation result of the lung segmentation to keep only the lung cavity. Basically, the GGO segmentation includes three major steps, namely attention mechanism threshold, contour equalization and lung segmentation. The approach was designed to handle low contrast CT images.

Note that only a few of the most representative works have been briefly reviewed here, dealing with CT images, while X - Ray image type works were excluded. The interested reader my consult the survey papers on the topic, where more approaches and details can be found. More precisely, the tremendous interest on this topic led to three overview papers, for each year, starting 2021. To date, there are three review papers concerning Covid-19 diagnosis models. [43] comprise a literature overview by 2021, whereas, [44] describe the models up to 2022. More recently, [45] cover a comprehensive review of the existing proposed models, including the year 2023.

Despite the DL success in general image classification, when it comes to COVID-19 infection region segmentation, the proposed DL or ML based models did not show their full potential, especially for the multi-class segmentation task. For example, in [15], the proposed approach led to an average Dice similarity coefficient (DSC) of only 0.54 and an average Sensitivity equal to 0.56. Similarly, [42] reported an average DSC of 0.59. These modest scores can be caused by several issues, as follows:

- The DL models are prone to overfitting for low number of training images. To reduce overfitting, many researchers applied transfer learning, where the networks were pretrained on general image segmentation (mostly on ImageNet data set) task without considering the particularities of Covid-19 lesions, such as low contrast between the lesion and tissue background or varying intensity inhomogeneities, thus limiting the potential of DL networks.

- The testing set is usually too small, due to the lack of sufficient data. For instance, in [42], the testing set had only 77 samples, whereas [15] had taken 48 samples for testing. As noticed by [44], the number of COVID-19 samples of more than 50% studies, out of 179 medical imaging-based automatic diagnosis models, is smaller than 50.

- A real-world Covid-19 lesion segmentation model should provide satisfactory performance regarding the data set sources type. This relates to cross-database validation performance, meaning that one system trained on a specific Covid-19 lesion data set performs well on a data set coming from different sources or CT hardware settings. Some data sets are coming in PNG graphical format [6], while others are coming from real CT sources. Moreover, some samples from several sources have lower contrast or are noisier than others coming from different data sets. Typically, the researches split each data set into training, validation and test, without considering training on one data set and testing on another test data set.

Compared to the existing studies, the main contributions of this work are as follows: 1) We employed a pre-processing step to remove the intralobular septal thickening and micro-vessels, to enhance the segmentation procedure; 2) A coarse GMM and/or multi-thresholding is derived to segment the full image into 3 ROIs, corresponding to lung, GGO and consolidation, respectively; 3) In the training phase, textural features are extracted from available ground-truth masked corresponding to each ROI and fed up to SVMs for learning; 4) The 2-nd step is a refinement procedure to validate or reassign each ROI to the correct label according to the SVMs output.

3 The proposed approach

Considering the limited number of samples, we propose an alternative to DL/ML systems that does not require any training procedure for the segmentation task. The key ingredient of the segmentation approach is the local region-based active contour model [46]. The main contribution of our work consists on:

- The vessels are removed from the initial CT images by combining a Hessian-based vesselness filter [47] with minimum moment of phase congruency covariance [48], that is robust against noise and also contrast insensitive. This pre-filtering step assures that most of the micro-vessels and intralobular septal thickening are suppressed.
- A first multi-level thresholding step is performed on vessels free CT images using electromagnetism optimization (MTHEMO), generating an initial coarse segmentation.
- The number of components (threshold levels), required by MTHEMO, is prior estimated by fitting a Gaussian mixture distribution (GMM), using an Expectation-Maximization (EM) algorithm.
- A multi-local region-based active contour model (mLR-ACM) is applied to ultimately segment the lesion in a fine-grained fashion.
- The mLR-ACM algorithm needs an initialization step. To automate this step, we formulate an automatic initialization procedure that relies on morphological skeleton of the MTHEMO based segmentation, by forming seed images.

Segmentation is a fundamental image processing task aims at isolating objects sharing common properties from a visual scene. The classical binary segmentation works by taking a threshold ("th") value and the pixels which intensity value is higher than "th" are labeled as the first class and the rest of the pixels correspond to a second class. One of the most used thresholding algorithms is based on the classical Otsu's method [49] that maximizes the variance between classes. The thresholding method is efficient for 2-class segmentation, but its complexity for multi-class segmentation increases exponentially with each new added threshold [50]. More recent, multi-thresholding (MTH) approaches involved evolutionary optimization methods in search for better threshold levels. In this paper we have used an electromagnetism optimization technique to find thresholds defining lung, GGO and Consolidation areas. This technique, named Multilevel Threshold based on the EMO algorithm (MTHEMO), was introduced by [51] for MT problem, which is a global optimization algorithm that mimics the electromagnetism law of physics. The approach employs an attraction-repulsion mechanism to evolve the members of the population guided by their objective function values. Otsu's objective function is used here, while other functions may exist, such as Kapur's method [51]. MTHEMO was reported to outperform the classical Otsu's technique, being robust against noise.

3.1 Micro-vessels removal

The lung elements of an axial slice of a CT scan may typically includes the five lobes, airways, basal and apical segments, trachea, aorta and micro-vessels. The blood vessels may appear as white branches, stripes or spots, characterized by high intensity pixels. Some other vessels may have low intensity, thus hardly visible, or some vessels may connect with similar high intensity pixels that form consolidation lesions, making them difficult to be delineated by simple histogram thresholding. To enhance the vessels pattern, CT image is filtered by computing the eigenvalues of the Hessian matrix (second order information of the gradient) [47] of the CT image. The method is addressing a specific local structure of the vessels, considering tubular shapes, measuring the contrast between the regions inside and outside of a specific range in the direction of the derivative. This can be accomplished by extracting the principal directions in which the local second order structure of the image can be decomposed, favouring the main orientation. A vesselness function is defined at different scales σ and in the neighborhood of a point $\mathbf{x}_o$ [47]:

$$\mathcal{V}_o(\sigma) = \begin{cases} 0, & \text{if} \lambda_2 > 0 \\ exp\left(-\frac{\mathcal{R}_{\mathcal{B}}^2}{2\beta_1^2}\right)\left(1 - exp\left(\frac{\mathcal{S}^2}{2\beta_2^2}\right)\right) \end{cases} \tag{1}$$

where $\mathcal{R}_{\mathcal{B}} = \lambda_1/\lambda_2$ corresponds to the blobness measure, accounting for the eccentricity of the second order ellipse that fits the vessel pattern, and λ_1 and λ_2 are the first eigenvectors of the Hessian $\mathcal{H}_{o,\sigma}$. β_1 and β_2 are thresholds that control the sensitivity of the filter. For an image of dimension d, the quantity S in eq. 1 refers to second order structureness, defined as:

$$\mathcal{S} = \|\mathcal{H}\|_F = \sqrt{\sum_{j \le d} \lambda_j^2} \tag{2}$$

This quantity tends to be low for smooth background with no change in contrast and the eigenvalues are small. We applied the method at four different scales.

3.2 Phase congruency

The Hessian-based vesselness filter does a descent job for stripe-like patterns, but performs poorly for detection of circle shaped blood vessels. To deal with circle-like blood vessels, the phase congruency model is applied. This is a frequency based model for which the edges are defined as the points were there is maximal order in the phase components of a frequency-based representation of the image.

The phase congruency (PhC_1) is defined as [48]:

$$PhC_1(x) = \frac{|E(x)|}{\sum_n A_n(x)} \tag{3}$$

where $|E(x)|$ is the local energy and $A_n(x)$ represents the Fourier amplitude at point (location) x of the image. When all the Fourier components are in phase congruency all the complex vectors (representing the Fourier components into the real-imaginary axes) are aligned and the ratio equals unity. On the other extreme, when there is no phase coherence the ratio drops down to zero. Kovesi extends the relation to account for noise variation, proposing the following variant:

$$PhC_2(x) = \frac{\sum_n W(x) \lfloor A_n(cos(\phi(x) - \overline{\phi}(x)) - |sin(\phi(x) - \overline{\phi}(x))|) - T) \rfloor}{\sum_n A_n(x) + \varepsilon}. \tag{4}$$

The term $W(x)$ is a weight term to moderate the frequency spread. The constant term ε is only introduced to avoid division by zero. T is a noise threshold and represents the estimated noise influence which is determined from the statistics of the filter response to the data. Only energy values that exceed T are counted for the output. The symbol $\lfloor \rfloor$ denotes that the enclosed quantity is equal to itself when its value is positive, and zero otherwise.

To link the variation of PhC_2 with feature orientation Or, one need to compute phase congruency independently in each orientation, compute moments of phase congruency and look at the variation of the moments with orientation. The principal axis, corresponding to the axis about which the moment is minimized, provides an indication of the orientation of the feature, whereas the magnitude of the maximum moment, corresponding to the moment about an axis perpendicular to the principal axis, gives an indication of the significance of the feature. Given an orientation set $OR = \{Or_j, j = 1, \ldots, p\}$, the maximum moment is defined by:

$$M = \frac{1}{2}\left(c + a + \sqrt{b^2 + (a-c)^2}\right), \tag{5}$$

where the quantities a, b and c are expressed as:

$$a = \sum_{j=1,\ldots,p} (PhC_2(\theta)cos(\theta))^2_{Or_j}, \tag{6}$$

$$b = 2 * \sum_{j=1,\ldots,p} (PhC_2(\theta)cos(\theta)) * (PhC_2(\theta)sin(\theta))_{Or_j}, \tag{7}$$

$$c = \sum_{j=1,\ldots,p} (PhC_2(\theta)sin(\theta))^2_{Or_j}\,, \tag{8}$$

By computing the maximum moment of phase congruency covariance, the weak (low contrast) edges are found and can be suppressed from the CT images, resulting a vessel-free image. It is worth mentioning that the phase congruency is contrast invariant.

Algorithm 1 Micro-vessels removal algorithm

Input: CT Image CI, scale (sigma) set $\sum = \{\sigma_i,\ i = 1,\ldots,k\}$, β_1, β_2, orientation set $OR = \{Or_j,\ j = 1,\ldots,p\}$

Output: Vessel free CT image - VFI

For each scale σ_i:
  Compute the second order derivative of the image (Hessian) $\mathcal{H}_{\sigma_i}$,
  Compute the first two eigenvalues λ_1 and λ_2 of $\mathcal{H}_{\sigma_i}$,
  Compute the filtered image $\mathcal{V}(\sigma_i)$ via relation 1, at each scale σ_i,
Form the final filtered image as $\mathbf{FI} = \arg\max_{\sigma_i \in \sum}\{\mathcal{V}(\sigma_i)\}$
Subtract **FI** from the original CT image, i.e. $\mathbf{SI} = \mathbf{CI} - \mathbf{FI}$
For each orientation Or_j
  Compute the phase congruency image PhC_2 from **SI** via relation 4,
Apply 6, 7, and 8 to compute the maximum momentum 5, **M**.
Binarize **M** to yield **BM**,
Element-wise multiplication between **SI** and **BM**, to obtain the vessel free image **VFI**.
Return VFI.

3.3 Electro-magnetism optimisation based multithresholding algorithm

Once most of the vessels were suppressed, a Multilevel Threshold based on the EMO algorithm (MTHEMO) [51] is used to yield a coarse segmentation. This step helps in building the seed image for the final fine-grained segmentation. The EMO algorithm is an iterative technique that searches to find a global solution of a nonlinear optimization problem. It starts by creating an initial population $\mathbf{S}_t = \{x_{1,t}, x_{2,t}, \ldots, x_{N,t}\}$ of lengthy N from n dimensional points xi, t at iteration t. These points are randomly picked up as initialization from a search region $\mathbf{X}$. At each iteration, EMO consists of two steps. In the first step, each point in $\mathbf{S}_t$ moves to a location guided by an attraction-repulsion mechanism similar to a the electromagnetism principle [51]. In the second step, those points are further moved locally by a local search and then become members of $\mathbf{S}_t$ in the next $t+1$ iteration. Each point $x_{i,t} \in \mathbf{S}_t$ in the search space $\mathbf{X}$ is assumed as a charged particle, where the charge is derived from the objective function as:

$$q_{i,t} = exp\left(-n\frac{f(x_{i,t}) - f(x_t^B)}{\sum_{i=1}^{N} f(x_{i,t}) - f(x_t^B)}\right), \tag{9}$$

The points with larger values are assumed to have more charges, thus attracting other points in $\mathbf{S}_t$. The points with lower value are assumed to have less charge and will repel other points in the set. Next, the force $F_{i,j}^t$ between two points $x_{i,t}$ and $x_{j,t}$ is computed as:

In our case the Otsu's objective function, 11. An objective function is set up to guide the evolution of the searching space. For a multilevel thresholding task (k thresholds), the problem can be formulated as:

$$\max_{\mathbf{TH}} \quad f(\mathbf{TH}) \quad \text{subject to} \quad \mathbf{TH} \in \mathbf{X}, \tag{10}$$

where $\mathbf{TH} = [th_1, th_2, \ldots, th_k]$ represents the intensity levels and $\mathbf{X}$ is the bounded feasible region constrained by the interval $0 - 255$.

As previously mentioned, Otsu's method is used as objective function, given by:

$$f(\mathbf{TH}) = \max\left(\sigma_B^2(TH)\right), \quad 0 \le th_i \le L-1, i = 1, 2, \ldots, k \tag{11}$$

with $L = 256$. Here $\sigma_B^2(TH)$ is the Otsu's variance for the level set **TH**. The complete population is represented by $\mathbf{S}_t = [\mathbf{TH}_1, \mathbf{TH}_2, \ldots, \mathbf{TH}_N]$. MTHEMO can be summarized as follows:

Algorithm 2 MTHEMO algorithm

Input: CT Image, threshold levels k
Output: Intensity threshold values $th_1, th_2, \ldots, th_k$

1: Compute the CT image histogram h
2: Compute the probability distribution P_h of the intensity values using h
3: Initialize the EMO parameters $Iter_{max}$, $Iter_{local}$, δ, k and N
4: Initialize a population S_t of N random particles with k dimensions
5: Compute ω_i (class probability) and μ_i (mean) for each class, then evaluate the objective function values $f(x_{i,t})$, for each point $x_{i,t}$
6: Compute a charge value $q_{i,t}$ assigned to each point $x_{i,t}$, then compute the force between two points $F_{i,j}^t$ and total force F_i^t, $i \neq j$.
7: Move the entire population S_t along the total force vector.
8: Apply the local search to the moved population and select the best elements of this search based on their objective function values.
9: Go to t = t + 1. If $t \geq Iter_{max}$ or if the stop criteria is satisfied then go to the next step. Otherwise, go to step 6.
10: Select the particle satisfying $x_t^B = \arg\max_{x_{i,t} \in \mathbf{S}_t}\{f(x_{i,t})\}$
11: **Return** $th_1, th_2, \ldots, th_k$, where each particle is associated to one threshold.

3.4 Localised edge-region-based active contour

The key ingredient of our approach consists on the method proposed by [46], a technique based on active contour model that spits an image into non-overlapping regions with the level-set functions (LSFs), where each segmented region represented as a zero level set has certain similar characteristics, in our case intensity similarities. Starting from an initial evolution curve, the local edge information is extracted from probability scores of a fuzzy k-nearest neighbor classifier and further used by the evolution curve to stop at boundaries of the region of interest. The diffusion direction of the evolution curve is controlled by a penalty term. This method can deal with intensity inhomogeneity, being also robust against image noise.

4 Experiments

To asses the performance of our proposed approach, the Italian Society of Radiology COVID-19 database has been used [53]. This version contains 829 CT images in jpg format. As the images come from CT slices, not all include Covid affected areas, and we picked up a subset of 310 images where the interested areas were present. For 1-class segmentation problem (presence or absence of infected areas), we compare the proposed approach with four segmentation models Inf-Net [54], Semi-Inf-Net [54], ACL [55] and MiniSeg [56]. Only for visualization purposes we also included two classical segmentation methods, U-Net [57], and U-Net++ [58]. We did not report evaluation results as these two methods yielded the worst output and were excluded. For the multi-class segmentation, we compare our approach with three DL models, namely DeepLabV3+ [59], FCN8s [60] and multi-class U-Net [57]. The steps for our approach are illustrated in Figure 1, for five CT images. Notice how one image enters an additional correction step to correct the estimate number of true statistical components. Figure 2 zooms in for clarity and details, stressing the consolidation and GGO areas. Running the correction step, the algorithm was able to correctly estimate the number of components, se depicted in Figure 3. Figure 4 shows visual comparison of 1-class lung for the various methods, while Figure 5 depicts visual comparison in the case of multi-class segmentation. Visually, our proposed approach is able to segment the infection with more accurate boundaries, compared to the other methods.

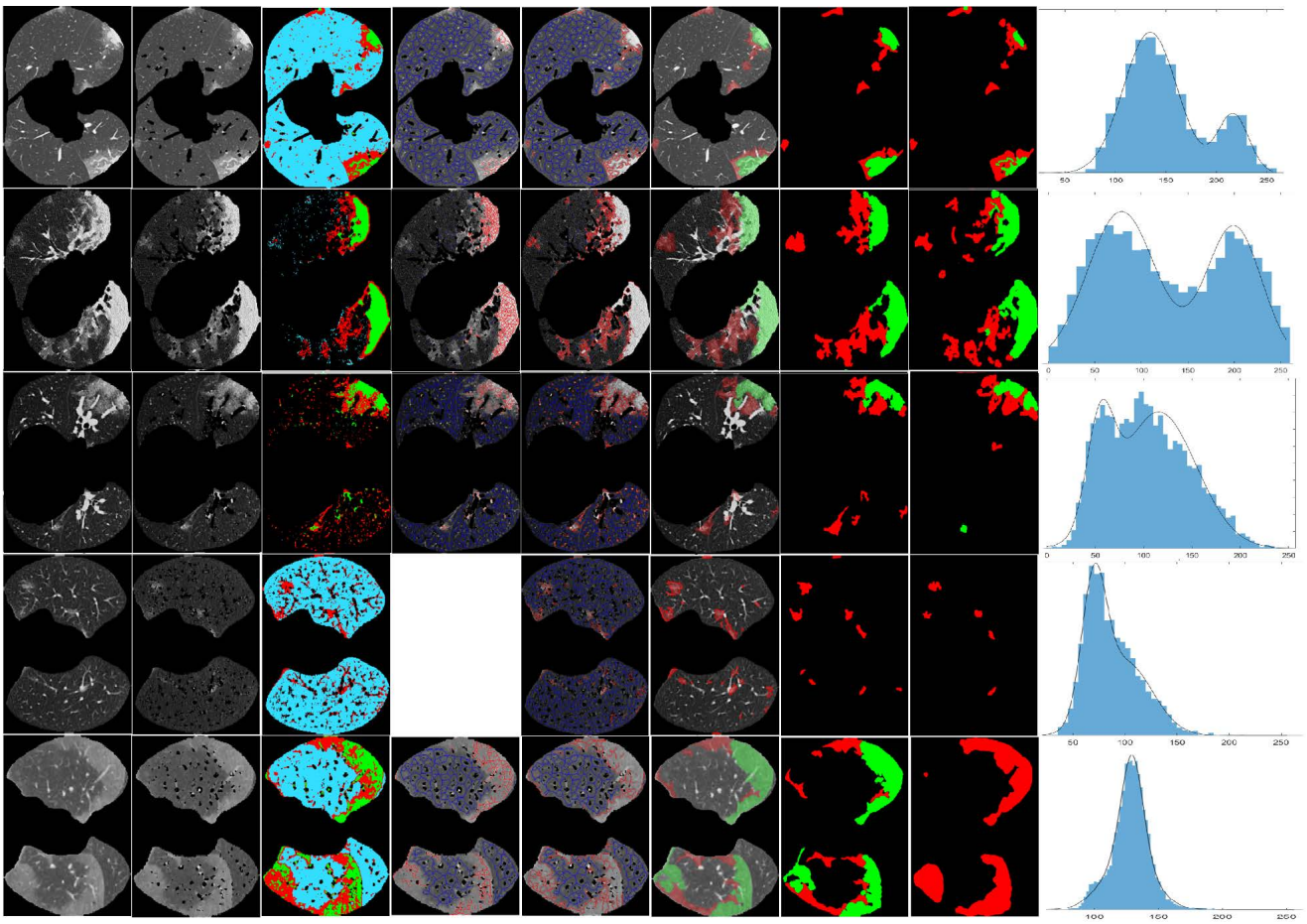

Figure 1: Steps visualization of our approach for five examples comming from database. From left to right: initial CT image, vessel free image, MTHEMO output with estimated NoC, seed image for consolidation, seed image for GGO, overlaid image, segmentation result, ground-truth, histogram of the segmented Covid affected region. If the histogram of the segmented lesion contradicts the estimated NoC, the algorithm runs again; for example, if the algorithm estimates NoC = 3 but the histogram has 2 peaks, or NoC = 4 but the histogram has only one peak. The first three rows correspond samples where NoC = 4, correctly estimated, the fourth row corresponds to NoC = 3, also correctly estimated, whereas the fifth row corresponds to a case where the number of components was wrongly estimated to 4. The true number of components is 3 (GGO only), indicated by the ground-truth and also confirmed by the 1-peak histogram of the segmented Covid affected region. This (fifth) example undergoes the correction step with output shown in figure 3. Note that, for the correct NoC = 3, there is no seed image for consolidation, represented by a blank image instead.

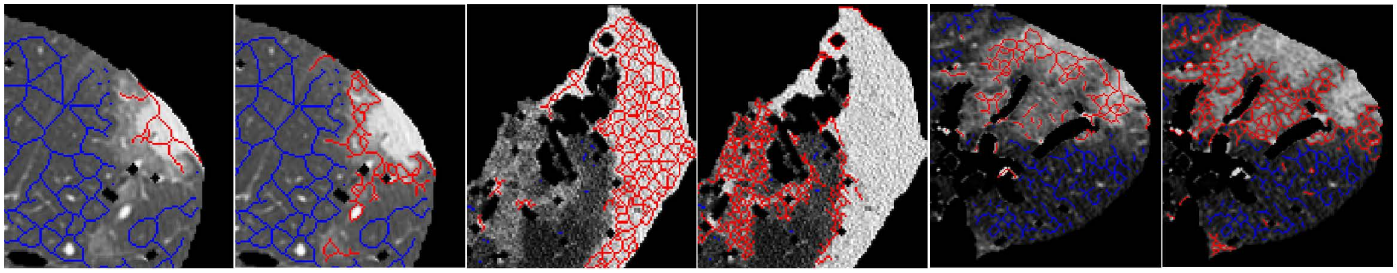

Figure 2: Close-up of seed images for the first three examples of figure 1. The images come in pair, where each odd image corresponds to consolidation, while the even image is associated to GGO. Blue and red skeleton refers to background (represented by lung here) and foreground (infected area as GGO or consolidation, respectively)

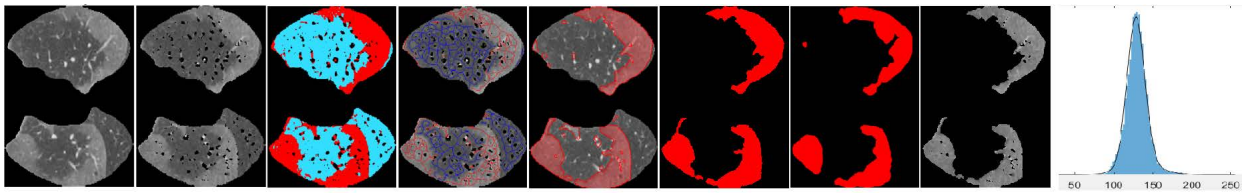

Figure 3: Correction step for the example from the fifth row of figure 1. Re-running the algorithm led to correct NoC. Notice, the similarity between the resulting histogram and that of figure 1.

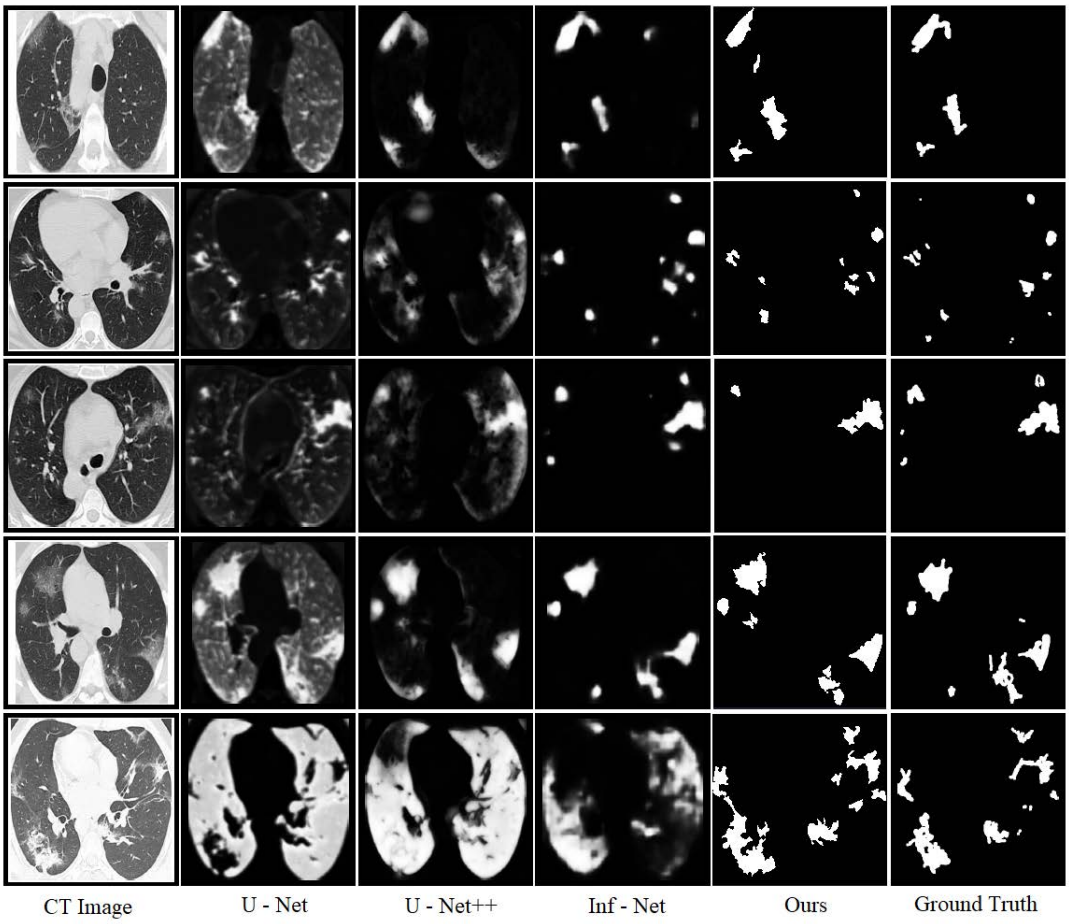

Figure 4: Visual comparison of 1-class lung infection segmentation results.

Five evaluation metrics were adopted to compare the performance of the proposed approach against the ground-truth. These are the following: Structure Measure, Mean Absolute Error (MAE), Sensitivity (Sen), Specificity (Spec), and Dice similarity coefficient (DSC).

Structure Measure S_α was proposed in [61] to measure the structural similarity between a prediction map S_p and ground truth mask G:

$$S_\alpha = (1-\alpha) * S_o(S_p, G) + \alpha * S_r(S_p, G) \tag{12}$$

where α is a balance factor between object-aware similarity S_o and region-aware similarity S_r. Here $\alpha = 0.5$. Mean Absolute Error is defined as the pixelwise error between S_p and ground truth mask G:

$$MAE = \frac{1}{w \times h} \sum_{x}^{w} \sum_{y}^{h} |S_p(x,y) - G(x,y)| \tag{13}$$

where w and h are the width and height of ground-truth G, and $(x; y)$ denotes the coordinate of

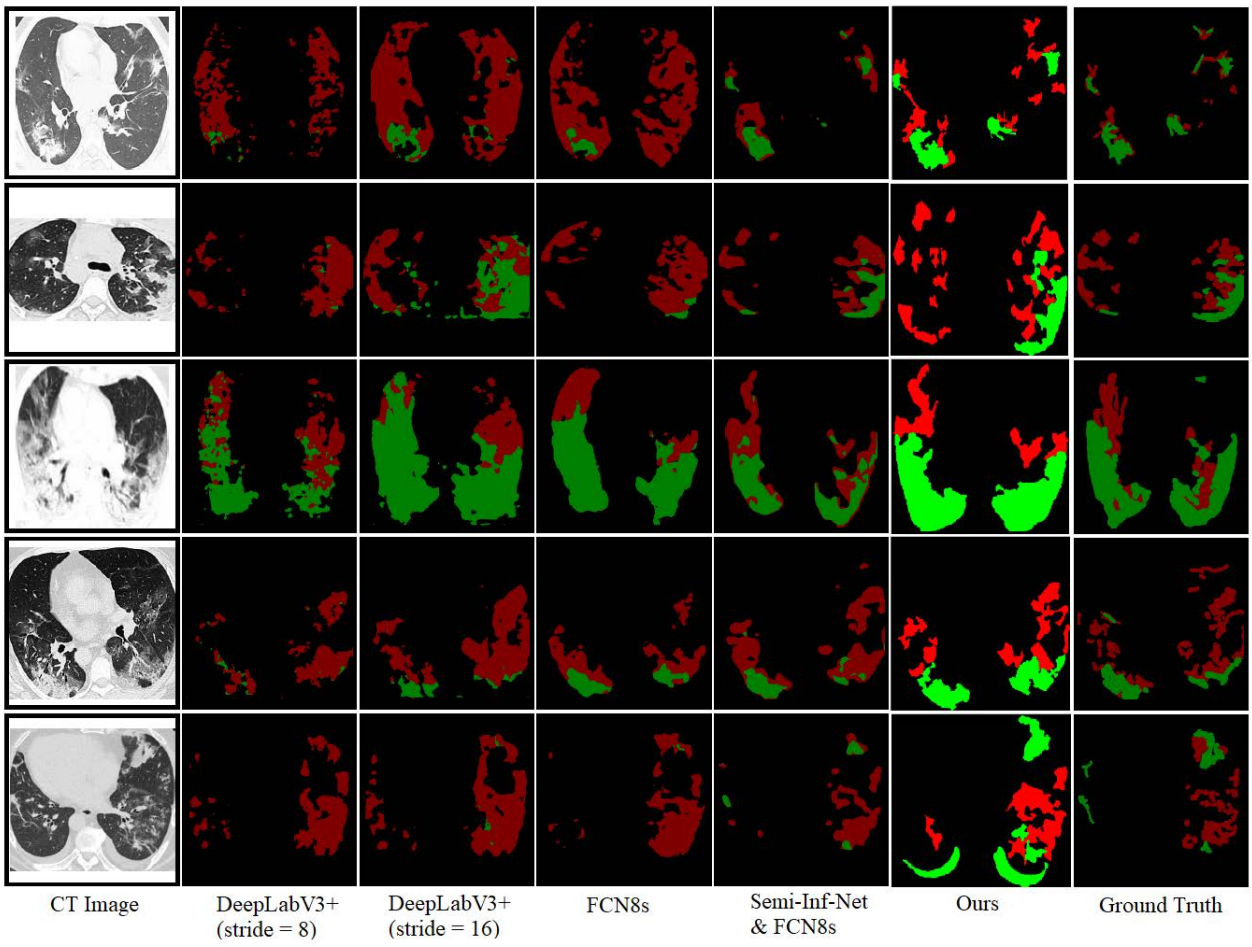

Figure 5: Visual comparison of multi-class lung infection segmentation results, where the red and green labels indicate the GGO and consolidation, respectively.

each pixel in G. DSC represents the overlap ratio between the prediction map S_p and ground truth mask G:

$$DSC = \frac{2 * |S_p \cap G|}{|S_p| + |G|} \tag{14}$$

We report the experiments only for 1 - class segmentation case, i.e. GGO and consolidation treated as one infection, all together. The output of the five metrics (mean values) for each method is tabulated in Table 1. The best results are in bold.

Table 1: Quantitative results for 1 - class segmentation task.

Method	S_α	MAE	meanSen	meanSpe	DSC
Inf-Net [54]	0.78	0.082	0.69	0.94	0.68
Semi-Inf-Net [54]	**0.80**	0.064	0.72	0.95	0.73
ACL [55]	0.72	0.010	0.58	**0.98**	0.62
MinSeg [56]	0.79	0.027	**0.83**	0.97	**0.75**
Ours	**0.80**	**0.009**	0.74	**0.98**	0.73

The experimental outcome indicates that the proposed approach is comparable in performance with the state-of-the DL methods for segmentation of medical images. It is worth noting that our approach led to the lowest MAE, similar to ACL. According to Table 1, Dice value is the second

highest for our approach, equally with Semi-Inf-Net. Remarkable, the specificity value placed the proposed method on top, sharing the position with ACL.

5 Conclusions

The COVID-19 pandemic term first used by the World Health Organization in March 2020 is still an issue, as the experts can't agree, in 2024, whether the disease is still a pandemic issue. Nevertheless, more cases are reported across the globe. As expected, the scientific community fights on every way to screen and detect infection from X-Rays or CT images. While promising results are publicly reported, lately using DL, the variety of image format and acquisition specs across the databases make this topic challenging. Moreover, DL based segmentation methods require large database, hardly accessible.

Perhaps, the most challenging factor in segmenting Covid-19 infections from CT images is given by the fact that, as mentioned before, the infected area is scarce and non-homogenous, limiting the accuracy of DL based segmentation methods. If we extend the task to general medical image segmentation, the situation does not improve. AI research exploaded and led to a foundation model called Segment Almost Anything (SAM) as a generic image segmentation model trained on the large visual corpus [62]. Despite remarkable performance in natural image segmentation, SAM may fail or perform poorly, as reported in [63].

To overcome the limitation of those methods, our proposed approach adopted several steps in segmenting non-homogenous areas in CT lung images, such GGO and consolidation caused by Covid virus infection. When compared to DL based state-of-the-art methods, our approach provides at least as good performance as the DL competitors, having the advantage of not requiring training.

Acknowledgments

The research has been funded by the University of Oradea, within the Grants Competition "Scientific Weak - May 21, Research Grant", Project No. 122/25.06.2021

Conflict of interest

The authors declare no conflict of interest.

References

[1] M.-Y. Ng et al. "Imaging Profile of the COVID-19 Infection: Radiologic Findings and Literature Review," *Radiology: Cardiothoracic Imaging.*, vol. 2, no. 1, e200034, Feb. 2020.

[2] Q. Hu, H. Guan, Z. Sun, L. Huang, C. Chen, T. Ai, Y. Pan, and L. Xia, (2020) Early CT features and temporal lung changes in COVID-19 pneumonia in Wuhan, China, *European Journal of Radiology.*, vol. 128, Article ID 109017, 2020.

[3] S. Zhou, T. Zhu, Y. Wang, and L. Xia, (2020) Imaging features and evolution on CT in 100 COVID-19 pneumonia patients in Wuhan, China, *Eur Radiol*, vol. 30, pp. 4–9, 2020.

[4] Li, L. and Qin, L. and Xu, Z. and Yin, Y. and Wang, X. and Kong, B. and Bai, J. and Lu, Y. and Fang, Z. and Song, Q. and Cao, K. and Liu, D. and Wang, G. and Xu, Q. and Fang, X. and Zhang, S. and Xia, J. and Xia J, (2020) Using Artificial Intelligence to Detect COVID-19 and Community-acquired Pneumonia Based on Pulmonary CT: Evaluation of the Diagnostic Accuracy, *Radiology*, vol. 296, pp. 65–71, 2020.

[5] Cohen, J.P. and Morrison, P. and Dao, L., (2020) COVID-19 Image Data Collection, *arXiv:2003.11597*, 2020.

[6] J. Zhao and Y. Zhang and X. He and P. Xie, (2020) COVID-CT-Dataset: A CT Scan Dataset about COVID-19, *https://arxiv.org/abs/2003.13865*, 2020.

[7] M. E. H. Chowdhury and T. Rahman and A. Khandakar and R. Mazhar and M. A. Kadir and Z. B. Mahbub and K. R. Islam and M. S. Khan and A. Iqbal and N. Al-Emadi and M. B. I. Reaz, (2020) Can AI help in screening Viral and COVID-19 pneumonia?, *https://arxiv.org/abs/2003.13145*, 2020.

[8] Li, Z. and Zhong, Z. and Li, Y. and Zhang, T. and Gao, L. and Jin, D. and Sun, Y. and Ye, X. and Yu, L. and Hu, Z. and Xiao, J. and Huang, L. and Tang, Y., (2020) From community-acquired pneumonia to COVID-19: a deep learning–based method for quantitative analysis of COVID-19 on thick-section CT scans, *Eur Radiol.*, vol. 30, pp. 6828–6837, 2020.

[9] [Online]. Available: http://medicalsegmentation.com/covid19/ Accessed: 2023-06-19.

[10] Bai, H.X. and Wang, R. and Xiong, Z. and Hsieh, B. and Chang, K. and Halsey, K. and Tran, T.M.L. and Choi, J. W. and Wang, D.C. and Shi, L. B. and Mei, J. and Jiang, X. L. and Pan, I. and Zeng, Q. H. and Hu, P. F. and Li, Y. H. and Fu, F. X. and Huang, R. Y. and Sebro, R. and Yu, Q. Z. and Atalay, M. K. and Liao, W.H. (2020), Artificial Intelligence Augmentation of Radiologist Performance in Distinguishing COVID-19 from Pneumonia of Other Origin at Chest CT, *Radiology*, vol. 296, pp. 156–165, 2020.

[11] Chaganti, S. and Grenier, P. and Balachandran, A. and Chabin, G. and Cohen, S. and Flohr, T. and Georgescu, B. and Grbic, S. and Liu, S. and Mellot, F. and Murray, N. and Nicolaou, S. and Parker, W. and Re, T. and Sanelli, P. and Sauter, A.W. and Xu, Z. and Yoo, Y. and Ziebandt, V. and Comaniciu, D. (2020), Automated Quantification of CT Patterns Associated with COVID-19 from Chest CT, *Radiol. Artif. Intell.*, vol. 2, pp. e200048, 2020.

[12] Krizhevsky, Alex and Sutskever, Ilya and Hinton, Geoffrey E. (2012), ImageNet Classification with Deep Convolutional Neural Networks, In *F. Pereira and C.J. Burges and L. Bottou and K.Q. Weinberger (Ed.) Advances in Neural Information Processing Systems*, vol. 25, 2012.

[13] Wang, M. and Xia, C. and Huang, L. and Xu, S. and Qin, C. and Liu, J. and Cao, Y. and Yu, P. and Zhu, T. and Zhu, H. and Wu, C. and Zhang, R. and Chen, X. and Wang, J. and Du, G. and Zhang, C. and Wang, S. and Chen, K. and Liu, Z. and Xia, L. and Wang, W. (2020), Deep learning-based triage and analysis of lesion burden for COVID-19: a retrospective study with external validation, *Rancet Digit Health*, vol. 2, pp. e506-e515, 2020.

[14] Wang, J. and Bao, Y. and Wen, Y. and Lu, H. and Luo, H. and Xiang, Y. and Li, X. and Liu, C. and Qian, D. (2020), Prior-Attention Residual Learning for More Discriminative COVID-19 Screening in CT Images, *IEEE Transactions on Medical Imaging*, vol. 39, pp. 2572–2583, 2020.

[15] Fan, D-P. and Zhou, T. and Ji, G-P. and Zhou, Y. and Chen, G. and Fu, H. and Shen, J. and Shao, L. (2020), Inf-Net: Automatic COVID-19 Lung Infection Segmentation From CT Images, *IEEE Transactions on Medical Imaging*, vol. 39, pp. 2626-2637, 2020.

[16] Ronneberger, O. and Fischer, P. and Brox, T. (2015), U-net: Convolutional networks for biomedical image segmentation, *Proc. Int. Conf. Med. Image Comput. Comput.-assisted intervention*, 234–241, 2015.

[17] Wu, D. and Gong, K. and Arru, CD. and Homayounieh, F. and Bizzo, B. and Buch, V. and Ren, H. and Kim, K. and Neumark, N. and Xu ,P. and Liu, Z. and Fang, W. and Xie, N. and Tak, WY. and Park, SY. and Lee, YR. and Kang, MK. and Park, JG. and Carriero, A. and Saba, L. and Masjedi, M. and Talari, H. and Babaei, R. and Mobin, HK. and Ebrahimian, S. and Dayan, I. and Kalra, MK. and Li, Q. (2020), Severity and Consolidation Quantification of COVID-19 from CT Images Using Deep Learning Based on Hybrid Weak Labels, *IEEE J Biomed Health Inform*, vol. 24, pp. 3529–3538, 2020.

[18] Zheng, B. and Zhu, Y. and Shi, Q. and Yang, D. and Shao, Y. and Xu, T. (20220, MA-Net:Mutex attention network for COVID-19 diagnosis on CT images, *Appl Intell (Dordr)*, vol. 52, pp. 18115-18130, 2022.

[19] Alshazly, H. and Linse, C. and Barth, E. and Martinetz, T. (2021), Explainable COVID-19 Detection Using Chest CT Scans and Deep Learning, *Sensors*, vol. 21, 33440674, 2021.

[20] Qian, X. and Fu, H. and Shi, W. and Chen, T. and Fu, Y. and Shan, F. and Xue X. (2020), M3 Lung-Sys: A Deep Learning System for Multi-Class Lung Pneumonia Screening From CT Imaging, *IEEE J Biomed Health Inform.*, vol. 24, pp. 3539-3550, 2020.

[21] Goel, T. and Murugan, R. and Mirjalili, S. and Chakrabartty, DK. (2021), Automatic Screening of COVID-19 Using an Optimized Generative Adversarial Network, *Cogn Comput.*, vol. 24, pp. 1–16, 2021.

[22] Oulefki, A. and Agaian, S. and Trongtirakul, T. and Laouar, AK. (2021), Automatic COVID-19 lung infected region segmentation and measurement using CT-scans images, *Pattern Recognit.*, vol. 114, pp. 107747, 2021.

[23] Pham, TD. (2020), A comprehensive study on classification of COVID-19 on computed tomography with pretrained convolutional neural networks, *Sci Rep.*, vol. 10, pp. 16942, 2020.

[24] Saood, A. and Hatem, I. (2021), COVID-19 lung CT image segmentation using deep learning methods: U-Net versus SegNet, *BMC Med Imaging*, vol. 21, pp. 19, 2021.

[25] Peng, Y. and Zhang, T. and Guo Y. (2023), Cov-TransNet: Dual branch fusion network with transformer for COVID-19 infection segmentation, *Biomed Signal Process Control*, vol. 80, pp. 104366, 2023.

[26] Hu, H. and Shen, L. and Guan, Q. and Li, X. and Zhou, Q. and Ruan S. (2022), Deep co-supervision and attention fusion strategy for automatic COVID-19 lung infection segmentation on CT images, *Pattern Recognit.*, vol. 124, pp. 108452, 2022.

[27] Li, W. and Cao, Y. and Wang, S. and Wan, B. (2023), Fully feature fusion based neural network for COVID-19 lesion segmentation in CT images, *Biomed Signal Process Control*, vol. 86, pp. 104939, 2023.

[28] Ma, Y. and Zhang, Y. and Chen, L. and Jiang, Q. and Wei B. (2023), Dual attention fusion UNet for COVID-19 lesion segmentation from CT images, *J Xray Sci Technol.*, 2023.

[29] Xiaocong Chen and Lina Yao and Yu Zhang (2020), Residual Attention U-Net for Automated Multi-Class Segmentation of COVID-19 Chest CT Images, *2004.05645*, 2020.

[30] Wang, S. and Kang, B. and Ma, J. and Zeng, X. and Xiao, M. and Guo, J. and Cai, M. and Yang, J. and Li, Y. and Meng, X. and Xu, B. (2021), A deep learning algorithm using CT images to screen for Corona virus disease (COVID-19), *Eur Radiol.*, vol. 31, pp. 6096–6104, 2021.

[31] Yu-Huan Wu and Shang-Hua Gao and Jie Mei and Jun Xu and Deng-Ping Fan and Rong-Guo Zhang and Ming-Ming Cheng (2021), An Explainable COVID-19 Diagnosis System by Joint Classification and Segmentation, *IEEE Transactions on Image Processing*, vol. 30, pp. 3113–3126, 2021.

[32] Wu, X. and Chen, C. and Zhong, M. and Wang, J. and Shi, J. (2021), COVID-AL: The diagnosis of COVID-19 with deep active learning, *Med Image Anal.*, vol. 68, pp. 101913, 2021.

[33] Gao, K. and Su, J. and Jiang, Z. and Zeng, LL. and Feng, Z. and Shen, H. and Rong, P. and Xu, X. and Qin, J. and Yang, Y. and Wang, W. and Hu D. (2021), Dual-branch combination network (DCN): Towards accurate diagnosis and lesion segmentation of COVID-19 using CT images, *Med Image Anal.*, vol. 67, pp. 101836, 2021.

[34] Yang, D. and Xu, Z. and Li, W. and Myronenko, A. and Roth, HR. and Harmon, S. and Xu, S. and Turkbey, B. and Turkbey, E. and Wang, X. and Zhu, W. and Carrafiello, G. and Patella, F. and Cariati, M. and Obinata, H. and Mori, H. and Tamura, K. and An, P. and Wood, BJ. and

Xu, D. (2021), Federated semi-supervised learning for COVID region segmentation in chest CT using multi-national data from China, Italy, Japan, *Med Image Anal.*, vol. 70, pp. 101992, 2021.

[35] Feng Shi and Liming Xia and Fei Shan and Bin Song and Dijia Wu and Ying Wei and Huan Yuan and Huiting Jiang and Yichu He and Yaozong Gao and He Sui and Dinggang Shen (2021), Large-scale screening to distinguish between COVID-19 and community-acquired pneumonia using infection size-aware classification, *Physics in Medicine & Biology*, vol. 66, pp. 065031, 2021.

[36] Liu, C. and Wang, X. and Liu, C. and Sun, Q. and Peng, W. (2021), Differentiating novel coronavirus pneumonia from general pneumonia based on machine learning, *Biomed Eng Online*, vol. 19, pp. 66, 2021.

[37] Mortani Barbosa EJ, Jr. and Georgescu, B. and Chaganti, S. and Aleman, GB. and Cabrero, JB. and Chabin, G. and Flohr, T. and Grenier, P. and Grbic, S. and Gupta, N. and Mellot, F. and Nicolaou, S. and Re, T. and Sanelli, P. and Sauter, AW. and Yoo, Y. and Ziebandt, V,. and Comaniciu, D. (2021), Machine learning automatically detects COVID-19 using chest CTs in a large multicenter cohort, *Eur Radiol.*, vol. 31, pp. 8775–8785, 2021.

[38] Feng Z, Shen H, Gao K, Su J, Yao S, Liu Q, Yan Z, Duan J, Yi D, Zhao H, Li H, Yu Q, Zhou W, Mao X, Ouyang X, Mei J, Zeng Q, Williams L, Ma X, Rong P, Hu D, Wang W. (2021), Machine learning based on clinical characteristics and chest CT quantitative measurements for prediction of adverse clinical outcomes in hospitalized patients with COVID-19, *Eur Radiol.*, vol. 31, pp. 7925-7935, 2021.

[39] Halder, A. and Chatterjee, S. and and Dey, D. (2020), Superpixel and Density Based Region Segmentation Algorithm for Lung Nodule Detection, *Proc. 2020 IEEE Calcutta Conference (CALCON), Kolkata, India*, 511–515, 2020.

[40] Firdaus, Q. and Sigit, R. and Harsono, T. and Anwar, A. (2020), Lung Cancer Detection Based On CT-Scan Images With Detection Features Using Gray Level Co-Occurrence Matrix (GLCM) and Support Vector Machine (SVM) Methods, *Proc. 2020 International Electronics Symposium (IES), Surabaya, Indonesia*, 643–648, 2020.

[41] Yunbo Rao and Qingsong Lv and Shaoning Zeng and Yuling Yi and Cheng Huang and Yun Gao and Zhanglin Cheng and Jihong Sun (2023), COVID-19 CT ground-glass opacity segmentation based on attention mechanism threshold, *Biomedical Signal Processing and Control*, vol. 81, pp. 104486, 2023.

[42] Yin, S. and Deng, H. and Xu, Z. and Zhu, Q. and Cheng, J. (2022), SD-UNet: A Novel Segmentation Framework for CT Images of Lung Infections, *Electronics*, vol. 11, pp. 130, 2022.

[43] Mondal, MRH. and Bharati, S. and Podder, P. (2021), Diagnosis of COVID-19 Using Machine Learning and Deep Learning: A Review, *Curr Med Imaging*, vol. 17, pp. 1403–1418, 2021.

[44] Liu, F. and Chen, D. and Zhou, X. and Dai, W. and Xu, F. (2022), Let AI Perform Better Next Time — A Systematic Review of Medical Imaging-Based Automated Diagnosis of COVID-19: 2020–2022, *Appl. Sci.*, vol. 12, pp. 3895, 2022.

[45] Lasker, A. and Obaidullah, SM. and Chakraborty, C. and Roy, K. (2023), Application of Machine Learning and Deep Learning Techniques for COVID-19 Screening Using Radiological Imaging: A Comprehensive Review, *SN Comput Sci*, vol. 4, pp. 65, 2023.

[46] Liu, H-X. and Fang, J-X. and Zhang, Z-J. and Lin, Y-C. (2021), Localised edge-region-based active contour for medical image segmentation, *IET Image Processing*, vol. 15, pp. 1567-1582, 2021.

[47] Frangi, AF. and Niessen, WJ. and Vincken, KL. and Viergever, MA. (1998), Multiscale vessel enhancement filtering, *in MICCAI*, pp. 130-137, 1998.

[48] Kovesi, P. (1999), Image Features From Phase Congruency, *Videre: A Journal of Computer Vision Research*, vol. 1, 1999.

[49] Otsu, N. (1979), A Threshold Selection Method from Gray-Level Histograms, *IEEE Transactions on Systems, Man, and Cybernetics*, vol. 9, pp. 62-66, 1979.

[50] Snyder, W. and Bilbro, G. and Logenthiran, A. and Rajala, S. (1990), Optimal thresholding: a new approach, *Pattern Recognition Letters*, vol. 11, pp. 803–809, 1990.

[51] Olivaa, D. and Cuevas, E. and Pajares, G. and Zaldivar, D. and Osuna, V. (2014), A multilevel thresholding algorithm using electromagnetism optimization, *Neurocomputing*, vol. 139, pp. 357–381, 2014.

[52] Hullermeier, E. and Rifqi, M. (2009), A Fuzzy Variant of the Rand Index for Comparing Clustering Structures, *in Proc. IFSA/EUSFLAT Conf.*, pp. 1294-1298, 2009.

[53] [Online]. Available: https://www.eibir.org/covid-19-imaging-datasets/, Accessed on 10 August 2024.

[54] Fan DP, Zhou T, Ji GP, Zhou Y, Chen G, Fu H, Shen J, Shao L. (2020) Inf-Net: Automatic COVID-19 Lung Infection Segmentation From CT Images. *IEEE Trans Med Imaging*. 2020 Aug;39(8):2626-2637. doi: 10.1109/TMI.2020.2996645. PMID: 32730213.

[55] Rao Y, Lv Q, Zeng S, Yi Y, Huang C, Gao Y, Cheng Z, Sun J. (2023) COVID-19 CT ground-glass opacity segmentation based on attention mechanism threshold. *Biomed Signal Process Control*, 2023 Mar;81:104486. doi: 10.1016/j.bspc.2022.104486. Epub 2022 Dec 5. PMID: 36505089; PMCID: PMC9721288.

[56] Qiu, Yu and Liu, Yun and Li, Shijie and Xu, Jing. (2022) MiniSeg: An Extremely Minimum Network Based on Lightweight Multiscale Learning for Efficient COVID-19 Segmentation. *IEEE Transactions on Neural Networks and Learning Systems*, 2022.

[57] O. Ronneberger, P. Fischer, and T. Brox, (2015) U-Net: Convolutional networks for biomedical image segmentation, in *MICCAI*. Springer, 2015, pp. 234–241

[58] Z. Zhou, M. M. R. Siddiquee, N. Tajbakhsh, and J. Liang, (2019) UNet++: A nested U-Net architecture for medical image segmentation, *IEEE Transactions on Medical Imaging*, pp. 3–11, 2019.

[59] L.-C. Chen, Y. Zhu, G. Papandreou, F. Schroff, and H. Adam (2018), Encoderdecoder with atrous separable convolution for semantic image segmentation, in *ECCV*, 2018, pp. 801–818.

[60] J. Long, E. Shelhamer, and T. Darrell (2015), Fully convolutional networks for semantic segmentation, in *CVPR*, 2015, pp. 3431–3440

[61] D.-P. Fan, M.-M. Cheng, Y. Liu, T. Li, and A. Borji (2017), "Structure-measure: A new way to evaluate foreground maps, in *ICCV*, pp. 4548–4557.

[62] A. Kirillov, E. Mintun, N. Ravi, H. Mao, C. Rolland, L. Gustafson, T. Xiao, S. Whitehead, A. C. Berg, W-Y Lo, et al. Segment anything. arXiv preprint arXiv:2304.02643, 2023

[63] T. Chen, L. Zhu, C. Ding, R. Cao, S. Zhang, Y. Wang, Z. Li, L. Sun, P. Mao, Y. Zang, Sam fails to segment anything?–sam-adapter: adapting sam in underperformed scenes: camouflage, shadow, and more, arXiv preprint arXiv:2304.09148

Journal's webpage: http://univagora.ro/jour/index.php/ijccc/

This journal is a member of, and subscribes to the principles of,
the Committee on Publication Ethics (COPE).
https://publicationethics.org/members/international-journal-computers-communications-and-control

Cite this paper as:

Curila, S.; Buciu, I.; Grava, C.; Nistor Trip, D.; Straciuc, O.-M. (2024). COVID-19 lung infection segmentation from CT imaging using statistics and edge-region-based active contour, *International Journal of Computers Communications & Control*, 19(6), 6862, 2024.

https://doi.org/10.15837/ijccc.2024.6.6862